

Multistructured accretion flow of Sgr A* II: Signatures of a Cool Accretion Disk in Hydrodynamic Simulations of Stellar Winds

MAYURA BALAKRISHNAN,¹ CHRISTOPHER M. P. RUSSELL,² LIA CORRALES,¹ DIEGO CALDERÓN,³ JORGE CUADRA,^{4,5}
DARYL HAGGARD,⁶ SERA MARKOFF,⁷ JOEY NEILSEN,⁸ MICHAEL NOWAK,⁹ Q. DANIEL WANG,¹⁰ AND
FREDERICK BAGANOFF¹¹

¹*Department of Astronomy, University of Michigan, 1085 S. University, Ann Arbor, MI 48109, USA*

²*Department of Physics and Astronomy, Bartol Research Institute, University of Delaware, Newark, DE 19716, USA*

³*Hamburger Sternwarte, Universität Hamburg, Gojenbergsweg 112, D-21029 Hamburg, Germany*

⁴*Faculty of Liberal Arts, Universidad Adolfo Ibañez, Av. Padre Hurtado 750, Viña del Mar, Chile*

⁵*Millennium Nucleus on Transversal Research and Technology to Explore Supermassive Black Holes (TITANS)*

⁶*Department of Physics, McGill University, 3550 University Street #040, Montreal, QC H3A 2A7, Canada*

⁷*Anton Pannekoek Institute for Astronomy/GRAPPA, University of Amsterdam, Science Park 904, rm. C4.151 1098 XH Amsterdam, Netherlands*

⁸*Department of Physics, Villanova University, 800 Lancaster Avenue, Villanova, PA 19085, USA*

⁹*Department of Physics, Washington University at St. Louis, 1 Brookings Dr, St. Louis, 63130 MO, USA*

¹⁰*Department of Astronomy, University of Massachusetts Amherst, 710 North Pleasant Street Amherst, MA 01003, USA*

¹¹*MIT Kavli Institute for Astrophysics and Space Science, MIT, 70 Vassar St, Cambridge, MA 02139, USA*

ABSTRACT

Hydrodynamic simulations of the stellar winds from Wolf-Rayet stars within the Galactic Center can provide predictions for the X-ray spectrum of supermassive black hole Sgr A*. Herein, we present results from updated smooth particle hydrodynamics simulations, building on the architecture of Cuadra et al. (2015); Russell et al. (2017), finding that a “cold” (10^4 K) gas disk forms around Sgr A* with a simulation runtime of 3500 years. This result is consistent with previous grid-based simulations, demonstrating that a cold disk can form regardless of numerical method. We examine the plasma scenarios arising from an environment with and without this cold disk, by generating synthetic spectra for comparison to the quiescent Fe K α Sgr A* spectrum from *Chandra* HETG-S, taken through the *Chandra* X-ray Visionary Program. We find that current and future X-ray missions are unlikely to distinguish between the kinematic signatures in the plasma in these two scenarios. Nonetheless, the stellar wind plasma model presents a good fit to the dispersed *Chandra* spectra within $1.5''$ of Sgr A*. We compare our results to the Radiatively Inefficient Accretion Flow (RIAF) model fit to the HETG-S spectrum presented in Paper I and find that the Bayesian model evidence does not strongly favor either model. With $9''$ angular resolution and high spectral resolution of the X-IFU, *NewAthena* will offer a clearer differentiation between the RIAF plasma model and hydrodynamic simulations, but only a future X-ray mission with arcsecond resolution will significantly advance our understanding of Sgr A*'s accretion flow in X-rays.

1. INTRODUCTION

Sagittarius A* (Sgr A*), the supermassive black hole in the center of the Milky Way, is immersed in a complex, multi-phase gaseous medium, and surrounded by a parsec-scale nuclear star cluster (see Genzel et al. 2010, for a review). While most of the cluster is comprised of old stars (Nogueras-Lara et al. 2020), there is

also a young population, including some 30 Wolf-Rayet (WR) stars with orbits that extend as close as ≈ 0.05 pc from Sgr A* (Paumard et al. 2006; Lu et al. 2013). WR stars are evolved, massive stars, characterised by powerful stellar winds that have mass-loss rates $\dot{M} \sim 10^{-5} M_{\odot} \text{ yr}^{-1}$ and terminal speeds $v \approx 500\text{--}2500$ km s $^{-1}$ (Martins et al. 2007). The relatively small separation between the WR stars means that their stellar winds collide in relatively high-density shocks, producing plasma that reaches 10^7 K, emits in X-ray (Baganoff et al. 2003;

Quataert 2004; Wang et al. 2013), and is accreted onto the supermassive black hole (Cuadra et al. 2005).

The number of relevant wind sources and their non-trivial orbital distribution (von Fellenberg et al. 2018; Jia et al. 2023), makes this region hard to model analytically, in particular if we want to obtain the amount of gas available for accretion onto Sgr A*. Several studies have therefore relied on hydrodynamic simulations to model the gas dynamics of the material supplied by the WR stars orbiting Sgr A*. The predicted accretion rate arising from hydrodynamic simulations (Cuadra et al. 2015, hereafter C15) at the Bondi radius ($\sim 4 - 5''$, or 0.2 pc; $\dot{M}_{\text{SMBH}} \sim 10^{-6} M_{\odot} \text{ yr}^{-1}$) is in agreement with theoretical estimates based on X-ray observations at the same scale (Baganoff et al. 2003). Further numerical work has reached deeper into the Galactic center, by first running parsec-scale simulations of the stellar winds (Ressler et al. 2018, 2020a), and then zoom-in magnetohydrodynamic (MHD) and general relativistic magnetohydrodynamic (GRMHD) models of regions progressively closer to Sgr A* (Ressler et al. 2020b). While these simulations do not currently fit observations close to the event horizon (Event Horizon Telescope Collaboration et al. 2022), they provide a promising framework for understanding how the observed properties of the accretion flow came to be.

The simulations used in C15, Russell et al. (2017, hereafter R17), and Calderón et al. (2020) focus on the WR stars as they have the largest mass-loss rates of any stars in the region (Martins et al. 2007). There is likely some outflow produced by the accretion flow of Sgr A* itself, predicted by simulations (Ressler et al. 2018; Dexter et al. 2020; Chatterjee et al. 2021) and Radiatively Inefficient Accretion Flow (RIAF) models (e.g., Blandford & Begelman 1999). RIAFs are parameterized by mass accretion rate, $\dot{m} \propto r^s$, material density, $n \propto r^{-3/2+s}$, and temperature $T \propto r^{-q}$. Here, $s = 0$ corresponds to classical Bondi accretion and $s = 1$ indicates an inflow balanced by an outflow (Begelman 2012). Observational fits to the multiwavelength spectral energy distribution (SED) of Sgr A* and *Chandra* ACIS spectrum with RIAF models suggest varying s values, with $s \sim 0.05 - 0.3$ closer to the BH (Yuan et al. 2003; Ma et al. 2019) and $s \sim 0.6 - 1$ at the Bondi radius (Ma et al. 2019; Wang et al. 2013), demonstrating that this outflow is more prominent at higher radii. However, incorporating this outflow into WR simulations has minimal impact on the predicted X-ray spectral shape and only marginally reduces the X-ray flux compared to simulations without Sgr A* feedback (R17). Main sequence OB-star winds, with mass-loss rates three orders of magnitude smaller than the WR stars, may also affect

the net mass accretion rate in this region but are found to underpredict the accretion rate at the Bondi radius (Lützendorf et al. 2016). Therefore, we solely consider mass loss from WR stars for our analysis.

The WR stars alone are able to explain an exceptional amount of the observed behaviour in this region, namely the predicted emission fully explains the X-ray spectrum of Sgr A* (R17). R17 post-processed the simulations of C15 using radiative-transfer tools, producing synthetic X-ray maps and spectra. Analysis of the synthetic observations shows that the overall X-ray flux depends mostly on the mass-loss rates, while the spectral shape is determined by the wind velocities. R17 found that the models closely reproduce the 2-10 keV *Chandra* ACIS spectrum in the $2'' - 5''$ region. This is rather noteworthy, as the models take as input the stellar wind and orbital properties obtained from infrared observations (Paumard et al. 2006; Martins et al. 2007), and are therefore completely independent of the X-ray data they explain.

The stellar wind simulations predict other observed structures. Depending on the stellar wind collision properties, the plasma can be prone to instabilities and form dusty, gaseous blobs (Fritz et al. 2011; Peißker et al. 2023), which may explain some of the gaseous structure observed in infrared and radio in the same region (Gillesen et al. 2012). Moreover, the stellar winds can perturb some of the larger-scale gaseous streams reaching the central region (Wang et al. 2020) or the circumnuclear disk (Solanki et al. 2023). The mechanisms that enable cold and hot phase plasma structures to co-exist in this way remains a mystery.

There have been claims of detection of a cool ($\sim 10^4$ K) H30 α disk co-spatial with the $\sim 10^7$ K accretion flow. Murchikova et al. (2019) measured line shifts at 231.9 GHz with the Atacama Large Millimeter/submillimeter Array (ALMA), finding red- and blue-shifted components approximately 0.004 pc from Sgr A*. The estimated mass of this ionized disk structure is approximately $10^{-4} - 10^{-5} M_{\odot}$. These results were confirmed in Yusef-Zadeh et al. (2020), who also found these line shifts in H39 α , H52 α , and H56 α emission. However, Ciurlo et al. (2021) obtained observational upper limits for the undetected Br γ disk (~ 6000 K) that are 80 times lower than the expected emission given the H30 α flux. These authors also argue that a maser explanation for this discrepancy, proposed originally by Murchikova et al. (2019), is not consistent with the expected properties of the plasma nor with the putative disc geometry. The results in Ciurlo et al. (2021), however, are consistent with Br γ emission levels predicted by Calderón et al. (2020), who showed that running the simulations for long-enough timescales (> 3000 yr) leads

to the accumulation of a ≈ 0.01 pc cold gas disk ($\sim 10^4$ K) around Sgr A*. This study utilized `ramses`, which follows an Eulerian approach and incorporates adaptive mesh refinement (AMR) for increased resolution, identifying two distinct mass accretion phases: quasi-steady and disk regimes. The quasi-steady phase, characterized by $\dot{M}_{in} > \dot{M}_{out}$, eventually transitions into the disk phase when a bow shock facilitates rapid cooling, leading to the formation of a cold gas disk. This process results in increased rates of inflow and outflow, eventually reaching a balance where $\dot{M}_{in} \sim \dot{M}_{out}$, indicative of $s \sim 1$ as predicted by RIAF models. We note that this disk is not generated in another series of simulations (Ressler et al. 2018, 2020a), even after extending the simulation run time to 9000 yrs in the past (Ressler et al. 2020a). This discrepancy could be due to differences in the cooling prescriptions; the effect of cooling on the formation of this disk is investigated further in Calderón et al. 2024 (in prep).

To test whether the cold disk formed in Calderón et al. (2020) is an artifact of the grid-based approach, we extend the SPH simulations of R17 to a longer timescale of 3500 yr. In addition, we test whether we can identify signatures of the cool accretion disk in the particle-based simulations by examining the predicted X-ray emission in both plasma scenarios. Although the predicted “cold” ($\sim 10^4$ K) disc is not directly observable in X-rays, we wish to investigate whether its kinematics might leave a signature in the hot gas. *Chandra* HETG currently offers the best available spectral resolution combined with sub-arcsecond imaging resolutions, which is required to study the Sgr A* accretion flow. While the low-resolution spectrum from this dataset is reproduced by the stellar winds (R17), we leverage the legacy *Chandra* HETG-S dataset from Corrales et al. (2020) to test whether hydrodynamic simulations of shock-heated WR stellar winds are also able to reproduce the observed X-ray spectrum at the high spectral resolution offered by *Chandra*. The High Energy Transmission Grating Spectrometer (Canizares et al. 2005, HETGS) on *Chandra* disperses a fraction of the incoming photons, providing a high-resolution spectrum with a spectral resolution between 60–1000. It consists of two gold gratings, MEG (0.4–5 keV sensitive) and HEG (0.8–10 keV sensitive, $E/dE \sim 170$ at 6.7 keV). Here we focus on the Fe K α complex (~ 6.7 keV) of the Sgr A* accretion flow captured by the HEG (Corrales et al. 2020) to evaluate the possibility that the observed line structure is a direct probe of the velocity structure in the accretion flow.

In Section 2, we describe our methodology, with details on the hydrodynamic simulation of the Wolf-Rayet winds followed by how predicted HEG spectra are gen-

erated. In Section 3, we show our X-ray line profiles and results from fitting these predictions to the HEG data. We compare the stellar wind profiles to the best fits for a RIAF model, presented in a companion paper (Balakrishnan et al. 2024a, referred to hereafter as Paper I), and show micro-calorimeter predictions of these two models. We end with a summary of our results and conclusions.

2. METHODS

The quiescent high-resolution spectrum of Sgr A* was extracted from the 3 Ms *Chandra* (PIs: Markoff, Nowak, & Baganoff) campaign in 2012 in Corrales et al. (2020). After removing flares from the soft particle background and from Sgr A* itself, the exposure time totals to 2.55 Ms. The counts spectrum was created by using customized background extraction regions that exclude the nearby sources pulsar wind nebula PWN G359.945-0.045 and star cluster IRS 13E. This work focuses on the Fe K α complex, which is the strongest X-ray line emission feature from Sgr A*, and we accordingly utilize the spectrum only between 6.4 keV and 7.2 keV. See Corrales et al. (2020) for further details on the cleaning and production of the spectrum.

Figure 1 shows the counts histograms for the source (0–1.5''; in solid black) and background (1.5''–5''; in dashed blue) regions, for both the HEG +1 and -1 orders. The data are binned to a factor of 3 for visual clarity. Peaks around 6.7 keV are visible in the source regions; numerous other features suggest potential velocity or temperature variations, but might also arise from statistical noise. The velocity resolution of the *Chandra* HEG is $\Delta v \sim 1500 \text{ km s}^{-1}$, which is close to the maximum line-of-sight velocities seen in the stellar wind simulations, indicating we may be able to probe the complex velocity structure in the Sgr A* accretion flow with the high resolution spectrum. To examine whether these line features can be explained by a non-homogeneous, multi-temperature plasma with velocity features, we utilize updated simulations from C15 and R17. We calculate the expected X-ray emission generated by stellar winds for each of the source and background regions, and process this thermal emission, accounting for any effects induced by the HETG-S detector. See Paper I for more details regarding corrections made for HETG-S geometry.

2.1. Simulation Setup

This work utilizes simulations for the plasma environment of Sgr A* created by WR stars in the central parsec, as developed by C15 and R17. These simulations use the smoothed particle hydrodynamics (SPH) code

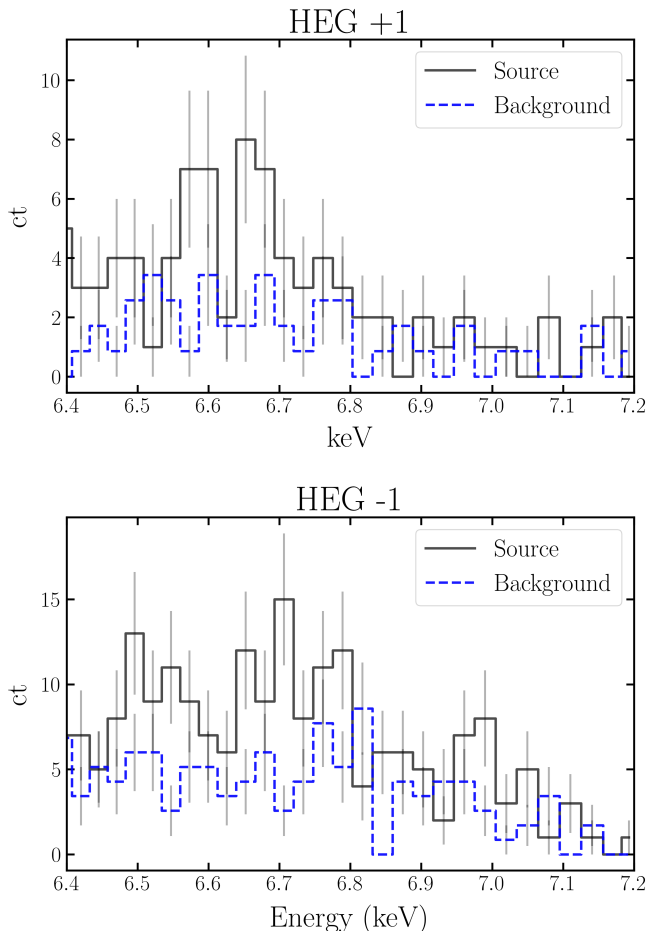


Figure 1. The high-resolution quiescent spectrum of Sgr A*, extracted in Corrales et al. (2020), plotted in counts. The top and bottom panels show the data from the HEG +1 and -1 orders, respectively. In this work, we focus on the Fe K α complex, between 6.4 and 7.2 keV. The spectra extracted from the source (out to 1.5'') and background (between 1.5'' and 5'') regions are plotted in black and blue, respectively, and are rebinned to a factor of 3.

GADGET-2 (Springel 2005) to follow the orbits of the 30 WR stars around Sgr A*, all while ejecting their stellar winds into the simulation domain of a half parsec in radius. The WR stellar mass-loss rates, wind speeds, and spectral types come from Martins et al. (2007), and the stellar orbits are from Paumard et al. (2006). These supersonic winds collide with one another, creating a complex structure of cold, free-streaming winds and hot, post-shock gas that emits thermal X-rays. Material flowing towards the SMBH is removed from the simulation at an inner radius of $r_{\min} = 1.2 \times 10^{16} \text{ cm} \approx 10^4 R_g$ (where $R_g = GM_*/c^2$), corresponding to a projected angular distance of 0.02'' from Sgr A* while material flowing outward is removed at $r_{\max} = 1.2 \times 10^{18} \text{ cm} \approx$

$2.4 \times 10^6 R_g$, corresponding to a projected angular distance of 12''.

In order to reproduce the work of Calderón et al. (2020), which found two different accretion modes onto Sgr A* (quasi-steady and disk mode), we perform two sets of simulations that have different initial starting times. Starting from 3500 yr (as done in Calderón et al. 2020) in the past yields a cold disk around the SMBH, while starting from 1100 yr ago (as done in C15) does not. Additionally, compared to the C15 simulations, the SMBH mass has been updated to $M_{\text{SMBH}} = 4.28 \times 10^6 M_\odot$ (Gillessen et al. 2017), and the separation of the WR stars in the IRS 13E cluster has been increased to bring the cluster's X-ray flux into better agreement with the observations (R17; see also Wang et al. 2020). We note that this mass is slightly different to that used in Paper I ($M_{\text{SMBH}} = 4.15 \times 10^6 M_\odot$; GRAVITY Collaboration et al. 2019); however, changing the mass in the RIAF model to match Gillessen et al. (2017) changes the counts histogram by less than 4%. These versions of the simulations do not take feedback from the SMBH into account; as shown in R17, this feedback does not change the shape of the X-ray spectrum significantly. The simulations include the same radiative cooling prescription as C15, which uses a $Z = 3Z_\odot$ cooling curve for all winds.

We can predict the HEG spectra from both sets of simulations to see if we can distinguish between the two accretion modes with X-ray spectra. A model spectrum for the thermal X-ray emission is synthesized from the hydrodynamic simulations in a similar fashion as R17, which is built upon a modified version of the visualization program *Splash* (Price 2007). All mass elements hot enough to emit thermal X-ray emission over $\sim 10^6$ K (indicated by superscript k) are assigned energy-dependent X-ray emissivities, $j_E^k = n_e^k n_i^k \Lambda(E, T^k)$ from the *vvapec* model (Smith et al. 2001) (obtained from XSPEC, Arnaud 1996). The temperature and emission measure of each mass elements' *vvapec* spectrum $\Lambda(E, T^k)$ corresponds to the temperature (T^k) and density (electron number density n_e^k and ion number density n_i^k) of the mass element computed in the hydrodynamic simulation. To distinguish between the various abundances of the winds, the winds and their *vvapec* spectra are split into three categories: WC8-9 stars, WN6-7 stars, and WN8-9 & Ofpe/WN9 stars (following R17). The optical depths through the simulation domain ($\int \kappa_E \rho^k dz$ with z being the line-of-sight integration direction) in the observed X-ray energy range are in the optically thin limit; this calculation made use of X-ray opacities (κ_E) of Verner & Yakovlev (1995) obtained

via an abundance-modified version of the `windtabs` model (Leutenegger et al. 2010).

While the density and temperature of the plasma is set by the hydrodynamic simulations, which use a $3 Z_{\odot}$ cooling prescription, our predicted Iron line profiles were calculated with abundances of $Z_{Fe} = 0.6 - 1 Z_{\odot}$ (Asplund et al. 2009) depending on the specific WR subtype (see Table 1 of R17 for details). A high metal abundance in the plasma is well-justified; WR stars have low (or non-existent) Hydrogen abundances but high Carbon, Nitrogen, or Oxygen abundances (Sander et al. 2019). Being young stars, WR stars are indicators of recent star formation, so it is reasonable to expect an Iron abundance $\sim Z_{\odot}$ or higher in the X-ray emitting plasma due to past stellar explosions. However, X-ray studies of WR stars are rare, and there is not yet a generally accepted value. Recent spectral fitting of the 6.7 keV line in the S 308 bubble around a galactic WR system finds a Nitrogen abundance of $\sim 3 Z_{\odot}$ and an Iron abundance consistent with $1 Z_{\odot}$ (Camilloni et al. 2024). Other studies have used Iron abundances as low of $0.4 Z_{\odot}$ (Sander et al. 2019). These abundances are similar to those found from fits to the X-ray emitting plasma around Sgr A*. The RIAF fit from Wang et al. (2013) found an Iron abundance of $Z_{Fe} = 1.23 Z_{\odot}$ (Asplund et al. 2009), while in Paper I, we found that the spectrum was best-fit an average Iron abundance of $Z_{Fe, \text{ Paper I}} = 0.18 Z_{\odot}$ (relative to Asplund et al. 2009, ; see Section 3.2 for further discussion).

We calculate the thermal X-ray intensity from the Sgr A* plasma with the X-ray emissivities above, while incorporating the line-of-sight velocities (v_{LoS}) in each plasma element. The profile function for mass element k is a Gaussian of the form:

$$\phi^k(v_{\text{LoS}}) = \frac{1}{\sqrt{\pi}} \exp\left(-\frac{(v_{\text{LoS}}^k - v_{\text{LoS}})^2}{v_{\text{th}}^2}\right) \quad (1)$$

where v_{LoS}^k is the element’s line-of-sight velocity, v_{LoS} is the particular line of sight velocity being computed, and v_{th} is the thermal/sound speed. `Splash` sums the contribution of each mass element across the $\{x, y\}$ pixel map to obtain thermal X-ray intensity at a particular energy, and we incorporate v_{LoS} as follows:

$$I_E(x, y) = \int j_E^k(x, y) dz = \int n_e^k n_i^k \Lambda(E, T^k) \phi^k(v_{\text{LoS}}) dz \quad (2)$$

where we integrate z , or line-of-sight direction, from $-2.4 \times 10^6 R_g$ to $2.4 \times 10^6 R_g$ where Sgr A* is situated in the plane of $z = 0$. Computing a single energy’s line profile requires looping over the full range of v_{LoS} , which ranges from -3000 to 3000 km s^{-1} in the simulation. The Fe complex has many lines that overlap each other when

their v_{LoS} ranges are converted to energy space, so we compute a line profile for each entry in the VVAPEC tables, yielding 150 line profiles at an energy resolution of 6400/dex. All of these overlapping line profiles are then finely interpolated to the same energy grid, where they are summed to yield the complete v_{LoS} -dependent spectrum in the Fe complex. Similarly, in the continuum region, calculations at specific energies blend into adjacent lines due to their proximity, resulting in a composite spectrum. Therefore, we conduct comprehensive line profile calculations across every point within both the continuum and line-complex regions to account for their influence on one another.

In Figure 2, we show the column density, X-ray intensity, and velocity maps corresponding to the disk (top row) and no-disk plasma scenarios (bottom row). Large scale density and X-ray emissivity field differences are at least in part due to the different run times, with the top row showing a snapshot at $t = 3500 \text{ yr}$ and the bottom row reflecting the plasma conditions at $t = 1100 \text{ yr}$. The disk is visible in the top left plot owing to its high column density. Contributions from slower winds result in high density shocks that cool radiatively, resulting in instabilities that lead to clumpy structure seen in the images. To make the velocity maps, we split the X-ray emission of the same line into 5 km/s bins for each pixel’s v_{LoS} . Subsequently, we assigned colors to each pixel based on the v_{LoS} corresponding to the maximum velocity-binned X-ray emission, utilizing a blue-white-red color gradient. Next, to highlight X-ray bright areas and consequently identify X-ray dim regions, we combined this color-coded v_{LoS} image with a grayscale image representing X-ray brightness. This process preserves the X-ray bright sections of the velocity map while enhancing the contrast of the X-ray dim areas. The disk and quasi-steady accretion scenarios lead to different kinematics in the gas that might be resolvable with the high-resolution *Chandra* spectrum.

2.2. Modeling the HEG spectrum

To calculate the predicted spectrum from the plasma surrounding Sgr A*, we only include emission from regions physically probed by the HEG (described in Paper I). We also incorporate extinction from the interstellar medium (ISM). We calculate the predicted HEG spectrum for the +1 and -1 orders separately instead of combining them due to the differences in the instrumental response matrices, which would be more apparent in this low count regime. The background regions extracted from Corrales et al. (2020) were stacked by roll angle, with the background “up” or “down” regions (in the cross-dispersion direction) opposite from PWN

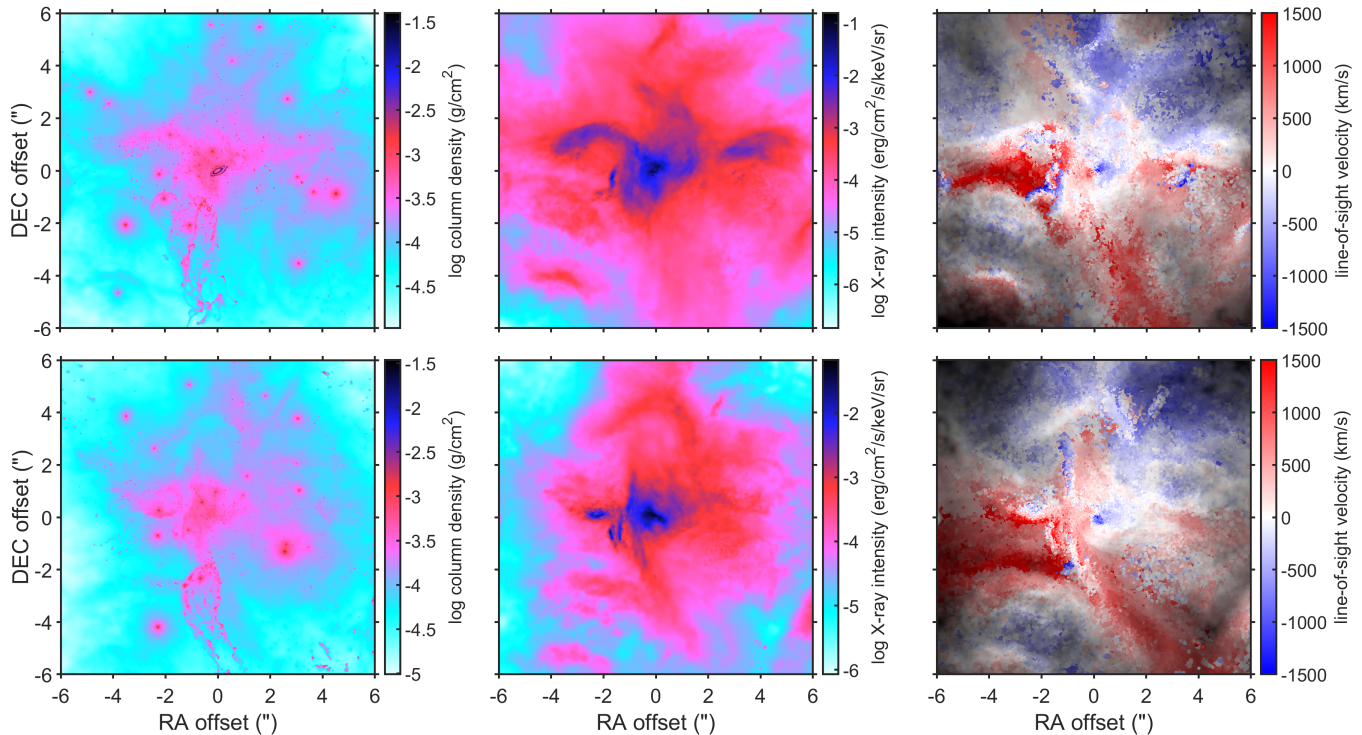


Figure 2. The top and bottom rows show the results of the disk (runtime of 3500 yr) and no-disk (runtime of 1100 yr) scenarios, respectively, for gas emitting at 6.7 keV. The plots span the central $12'' \times 12''$ surrounding Sgr A*, with North upwards and East to the left. LEFT: Column density map of the region, with the cool disk of gas seen clearly in the top left panel. MIDDLE: 6.7 keV X-ray intensity with the dark blue highlighting high levels of Fe K α emission. RIGHT: Illustration of the velocity structure in this complex plasma, with color denoting the line-of-sight velocity corresponding to the line profile’s maximum X-ray brightness for each pixel. The grayscale overlay reflects X-ray emission intensity, i.e. dimmer regions indicate X-ray dim gas.

G359.95-0.04 and IRS 13E, chosen to minimize contamination. Since the simulated stellar wind plasma is not radially symmetric, we slice the annular region in half along galactic coordinates; Galactic North refers to regions where $b > 0$ and Galactic South refers to regions where $b < 0$. These two halves roughly correspond to the background regions considered. We use the spectrum calculated solely from the Galactic South as our background model, which ensures that we are capturing the plasma that is opposite in projection from PWN G359.95-0.04 and IRS 13E.

The standard spectral extraction for HETG-S data captures X-ray events within a $1.5''$ radius in the dispersion direction and $3''$ along the dispersion axis¹. The source region, with a $1.5''$ radius, is fully encompassed within the projected HETG extraction area. However, the background region extends beyond $1.5''$ in the cross-dispersion direction. Accordingly, we introduce a scaling factor to the predicted background spectra denoting the area captured by HETG, which is the ratio of the

background extraction region to the Galactic South half-annulus region described above ($f_B = 0.3$).

Following the procedure described in Section 3.2 of Paper I, we take into account the slitless nature of the HETGS by implementing a powerlaw background model. We include extinction due to the interstellar medium, employing the ISM abundance table of Wilms et al. (2000) and the dust extinction cross-sections from the ISM_{dust} model (Corrales et al. 2016). We use the publicly available Python package `pyxsis`² to apply the instrumental response functions and perform a joint fit for the background models of the HEG +1 and HEG -1 spectra from Corrales et al. (2020).

3. RESULTS

We calculated line profiles from the two accretion modes (a disk versus a quasi-steady flow) that arise in the stellar wind simulations. We also compare the goodness-of-fit metrics for the stellar wind models with

¹ <https://cxc.harvard.edu/proposer/POG/html/chap8.html>

² <https://github.com/eblur/pyxsis>

the best fitting radiatively inefficient accretion flow (RIAF) model found in Paper I.

3.1. Searching For Signatures of a Cold Disk

There is evidence of a cold gas disk around Sgr A* that simulations demonstrate could arise from shocked stellar winds. Observations of H30 α emission indicate the presence of a cold disk of gas $\sim 10^4$ K that extends about $0.23''$ ($\sim 4.6 \times 10^4 R_g$) wide and is co-spatial within the hot accretion flow (Murchikova et al. 2019). Interestingly, this observed cooler gas disk rotates counter to the hot plasma, but aligns with the rotation of the Galaxy, the circumnuclear disk, the mini-spiral, and the clockwise stellar disk (Murchikova et al. 2019). We find that a cool disk naturally arises in the stellar wind plasma in both particle-based and grid-based simulations. However, in both cases, the simulated cold gas disk has an angular momentum vector offset by 90° orientation with respect to the observed disk. This misalignment suggests that other interacting structures, such as the minispiral or circumnuclear disk, which have not been incorporated into the simulations, may play a crucial role in its formation. This cold gas disk would not emit in the X-ray, but the presence of the cool disk heightens the accretion rate, resulting in slightly different plasma conditions (see Figure 2) which might be resolvable with X-ray spectroscopy. Differences in X-ray line profiles arising due to numerical method (i.e. particle-based vs. grid-based simulations) are investigated further in Calderón et al. 2024 (in prep).

To test whether we can resolve the differences between a hot plasma with and without a cool gas disk, we calculated the X-ray emission arising from both scenarios and generated predicted *Chandra*-HETG spectra. Figure 3 (left) compares the simulated X-ray gas emission arising from a plasma with and without a cold gas disk. The top row pertains to plasma within the source extraction region, ranging from $0''$ to $1.5''$, while the bottom row shows plasma within the Galactic South section of the background annulus, spanning from $1.5''$ to $5''$. Within the plots, the disk and no-disk scenarios are represented by solid and dash-dotted lines, respectively. Unfortunately, the HEG predicted spectra from the two accretion modes are almost indistinguishable. The distinction between the disk and quasi-steady flow scenarios is clearest in the Fe K α emission features, where the peaks are shifted, but not to a degree that can be easily resolved by *Chandra*. The maximum vertical difference between the two spectra is 2.6%. Therefore, our current dataset is not sufficient to differentiate between the different plasma conditions that arise in the disk accretion and quasi-steady flow modes. Given the observational

evidence of a cool accretion disk surrounding Sgr A* (Murchikova et al. 2019), we only consider the X-ray line profiles from the disk scenario, moving forward.

3.2. Stellar Winds vs. RIAF

In Paper I, we used `pyatomdb` to calculate the emission from plasma in Coronal Ionization Equilibrium (CIE) governed by density and temperature profiles according to the Radiatively Inefficient Accretion Flow (RIAF) parametrization (Yuan et al. 2003; Xu et al. 2006; Narayan et al. 2012). The main parameters are the slope of the temperature profile, q , and the steepness of the mass accretion rate and electron density, s . We also fit for the relative abundance of Iron in `pyatomdb`, leading to a total of three free parameters in our RIAF model: s , q , and Z_{Fe} . The predicted HEG spectrum was computed with the same method as the stellar wind emission, accounting for geometry, instrumental effects, and ISM extinction. A significant distinction between the RIAF and stellar wind models is that the former does not take into consideration any potential velocity structure inside the plasma, including rotation. This has limited impact on our results, as extinction coupled with the HEG instrument response wash out the fine structure (see Paper I for more details). A Monte-Carlo Markov Chain (MCMC) fit to the data yields best-fit and 90% credible intervals of $s = 0.74$ ($-0.12, +0.66$), $q = 0.22$ ($-0.22, +1.35$), and $Z_{Fe} = 0.13Z_\odot$ ($-0.10, +0.19$). The best-fit RIAF s value is roughly consistent with an inflow balanced by an outflow ($s \sim 1$). The data prefer a RIAF model with a low Iron abundance, where $Z < 0.3Z_\odot$.

Similarly, we use the publicly available `emcee` package to perform an MCMC fit for the background model with the static spectral model computed from the hydrodynamic simulations of WR stellar winds. The background contamination comes from different regions of the Galactic Center X-ray image, so the powerlaw parameters are allowed to be different for the +1 and -1 HEG orders, yielding a total of four free parameters.

We fit the source and background regions for both orders simultaneously, using Cash statistics. We initiated the model with 20 walkers and applied uniform priors of $-20 < \gamma < 20$ and $-12 < \log N_{PL} < -3$. We ran the MCMC chains until the autocorrelation time, which measures the number of steps required for the chain to achieve a state independent of its previous state, was less than 5%. The resulting best fits and 90% credible intervals for the powerlaw components are: $\log N_{PL,+1} = -7.6$ ($-0.1, +0.1$), $\gamma_{+1} = 6.7$ ($-6.7, +7.4$), $\log N_{PL,-1} = -7.2$ ($-0.1, +0.1$), $\gamma_{-1} = 4.1$ ($-3.8, +3.7$).

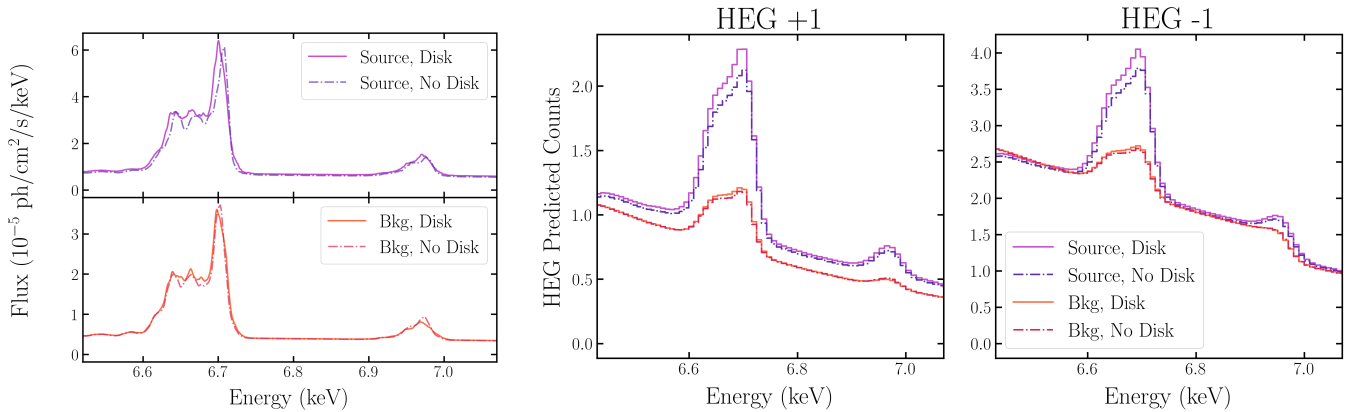


Figure 3. LEFT: Line profiles generated by plasma simulated in the $0''$ - $1.5''$ source region (top) and $1.5''$ - $5''$ background region (bottom). MIDDLE & RIGHT: Predicted counts histograms calculated for HEG +1 (middle) and HEG -1 (right) for the disk (solid curves) and no-disk (dashed curves) plasma scenarios in the stellar winds simulation. We plot the source and background regions in purples and reds, respectively. The small differences between the final spectra with and without a cold gas disk are slight and not resolvable with *Chandra*-HETG, differing only by $\sim 2.6\%$ at the peaks. We are thereby unable to detect evidence of the $\sim 10^4$ K disk from X-ray spectroscopy alone.

In Figure 4, we plot the stellar wind plasma model on top of the best-fitting background model (pink), best-fit RIAF from Paper I (blue), and the observed HEG spectra (black). We have binned the models and data to a factor of 4 for visual clarity, including the residuals. Focusing solely on the model counts histograms, it is intriguing that the simulation of stellar winds and the RIAF model both predict peaks in Iron at 6.7 keV with comparable strengths. The line intensity in the simulations is determined by assuming a plasma abundance of $0.6 - 1 Z_{\odot}$ (Asplund et al. 2009) depending on the specific WR subtype, whereas the RIAF fit yielded a lower value of $Z_{\text{Fe}} = 0.13Z_{\odot}$ (Anders & Grevesse 1989). Converting from Anders & Grevesse (1989) to (Asplund et al. 2009) yields a $Z_{\text{RIAF}} = 0.18 Z_{\odot}$ and a 90% credible upper limit of $0.45 Z_{\odot}$.

We investigated whether differences in the temperature and density profiles from both models could explain the lower metallicity predicted by the RIAF model. The WR plasma model predicts elevated plasma temperatures compared to the RIAF temperature profile. At higher temperatures, a higher fraction of the Iron will be in the Fe XXVI state, which reduces the strength of the 6.7 keV line complex. Therefore, the cooler temperatures in the RIAF model are able to produce the same strength 6.7 keV line with less total Iron abundance. One major difference between the RIAF and WR spectral models is that the WR plasma predicts a more significant 6.97 keV feature from Fe XXVI. We are unable to detect this feature in the HEG spectrum due to the very low effective area at this energy.

Examining the fits to the data, both models capture some of the features in the HEG +1 and -1 source spectra. However, the HEG -1 model spectra recreate nei-

ther the broadening in the 6.7 keV line nor the features at 6.5 and 7.0 keV. The background and extra features for the HEG -1 are likely influenced by its placement on a back-illuminated chip, which has a higher background, as opposed to rotation or other broadening effects inherent in the plasma. Both the simulations and the RIAF model anticipate a 6.7 keV feature in the background area that is not very pronounced, suggesting that other sources of photons are likely more dominant $3 - 10 \times 10^6 R_g$ away from Sgr A*. Indeed, the flux from the powerlaw contributes 95% - 98% of the flux in the background spectra.

In all procedures, the Cash statistic was used to evaluate goodness-of-fit in our MCMC sampling. Figure 5 shows the distributions of the Cash statistic resulting from fitting the stellar wind plasma (pink) and the RIAF model (blue). While the stellar wind plasma model may appear to offer a better fit, there is considerable overlap in the Cash statistic distributions. To evaluate which model is statistically preferred, we utilize the Bayesian model evidence.

Bayesian inference provides a consistent approach to the estimation of a set of parameters in a model H using Bayes' theorem (Feroz 2013). For a helpful overview of Bayesian inference in astronomy and variation in notation, see Eadie et al. (2023). Bayes theorem provides the probability distribution of model H parameters, Θ , given the dataset, D :

$$p(\Theta|D, H) = \frac{p(D|\Theta, H)p(\Theta|H)}{p(D|H)}. \quad (3)$$

On the left, $p(\Theta|D, H)$, we have the posterior distribution. On the right, $p(D|\Theta, H)$ is the model likelihood $\mathcal{L}(\Theta)$, for which we use the Cash statistic, and

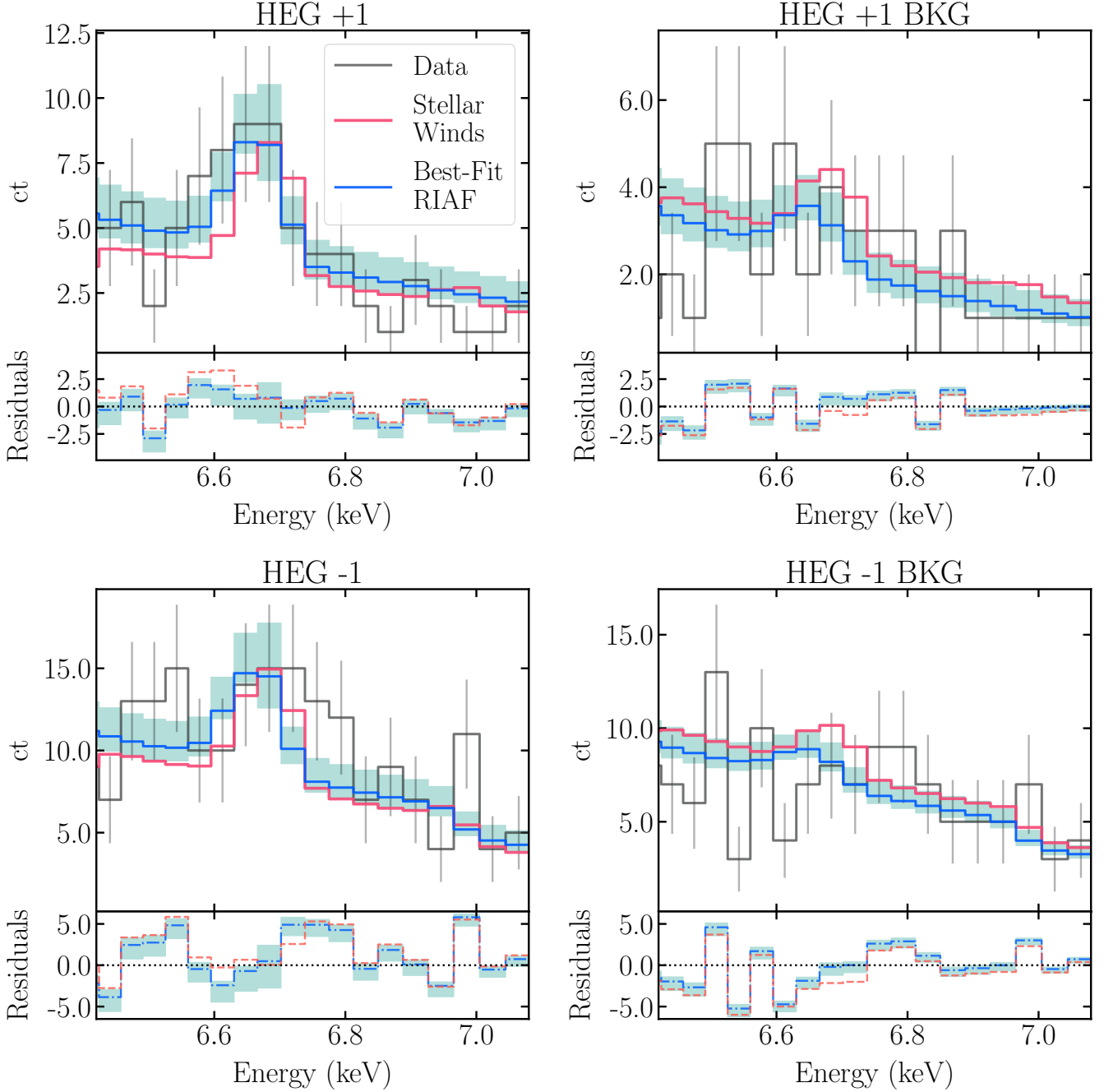


Figure 4. Final fits to the HEG +1 and -1 source and background regions. The observation is plotted in black, with the best-fit RIAF model in blue and the stellar wind simulations plotted in pink. The residual counts spectrum (observation – model) are plotted below each subplot. The data is binned to a factor of 4 for visual clarity, however, the fitting was performed on the unbinned HEG data. While the models capture the 6.7 keV peak in the source spectrum, most of the observed line structure is not predicted in the simulations.

$p(\Theta|H)$ is the prior for the model parameters. The denominator, $p(D|H)$, refers to the marginal likelihood or Bayes/model evidence. The Bayes evidence does not depend on the parameters, and is not used in parameter estimation, but is helpful when comparing two models. Selection between competing models H_0 and H_1 can be

done by comparing their respective posterior probabilities to compute the model odds (Bayes Factor), \mathcal{R} , as follows:

$$\mathcal{R} = \frac{p(H_1|D)}{p(H_0|D)} = \frac{p(D|H_1) p(H_1)}{p(D|H_0) p(H_0)}$$

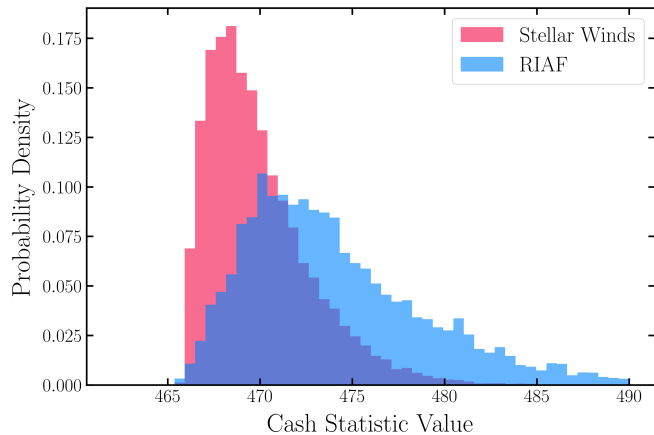


Figure 5. Histograms showing the Cash statistic from the posterior distributions of both the RIAF (blue) and stellar wind simulation fits (pink).

where $p(H_1)/p(H_0)$ is the prior probability ratio for the two models. Once the posterior has been determined, the model evidence, $p(D|H)$ can be evaluated numerically by integrating the likelihood over the prior: $p(D|H) = \int L(\Theta)p(\Theta|H)d^n(\Theta)$ over the parameter space. Calculating the Bayes evidence involves an integral that can be numerically challenging; several methods have arisen to address this (Feroz et al. 2009; Handley et al. 2015; Cai et al. 2021). We use the learnt harmonic mean estimator, which uses machine learning techniques to approximate the harmonic mean of posterior probabilities, providing a more efficient estimation method compared to traditional sampling (McEwen et al. 2021). By leveraging predictive models trained on observed data, it offers a more tractable computational solution for estimating the Bayesian evidence. We used the open source code `harmonic` (McEwen et al. 2021) to compute the model evidence and the Bayes Factor from the posterior samples calculated in our `emcee` runs. The Bayesian evidence is larger for a model if more of its parameter space has high likelihood values and smaller for a model with large areas in its parameter space having low likelihood values. Thus, using the Bayes evidence for model selection accounts for the differences in model complexity between our RIAF and stellar wind models. The value of the Bayes factor, \mathcal{R} , is often interpreted using Jeffreys’ scale (Jeffreys 1998; Lee & Wagenmakers 2013), where $0 < \log \mathcal{R} < 2$, $2 < \log \mathcal{R} < 6$, and $6 < \log \mathcal{R} < 10$ indicate the ranges for weak, moderate, and strong evidence for model H_1 over model H_0 , respectively. With H_1 denoting the RIAF model and H_0 denoting the stellar wind simulations, we find that $\log \mathcal{R} \sim 2$, indicating a weak favour towards the RIAF model. However, the Bayes evidence is not strong enough to support either model for the accretion flow of

Sgr A*. We note that non-linearities in the parameter space for the RIAF model make calculating the Bayes evidence challenging, adding to our conclusion the data do not strongly prefer either model.

3.3. Sgr A* at micro-calorimeter resolution

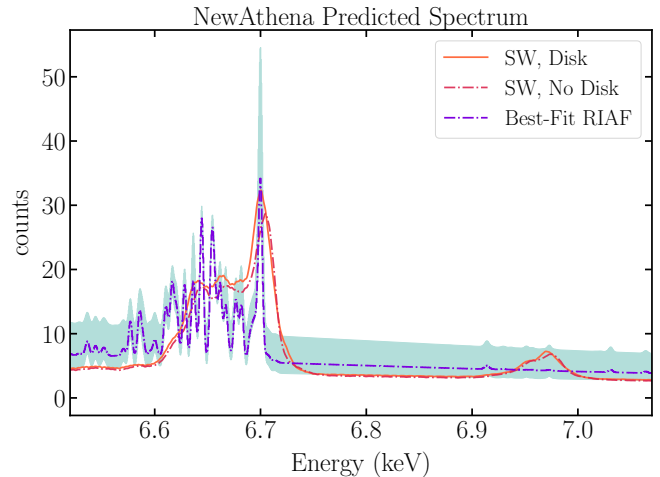


Figure 6. The anticipated *NewAthena* photon counts spectra for the stellar wind plasma models (red) under both disk (solid) and quasi-steady (dot-dashed) accretion scenarios in the Fe K α region. The best-fit RIAF and contours from Paper I are overlaid in blue. The stellar wind model will be differentiable from the RIAF model, and it is possible, with a high signal-to-noise, to detect signatures of the cold disk in the X-ray plasma.

While the *Chandra*-HETG is not able to strongly differentiate between the stellar wind plasma and a RIAF model, new and future missions, especially those utilizing microcalorimeters, could theoretically elucidate the mechanics at play. The HETG-S provides high spectral resolution for point sources, reaching ~ 60 - 70 eV at 6.7 keV, coupled with a spatial resolution of $0.5''$. The approved ESA L-class mission *NewAthena*, launching late 2030s, will have an imaging resolution of $9''$, and the X-IFU microcalorimeter will provide a spectral resolution of 4 - 5 eV at 6.7 keV.³ The advantages of microcalorimetry over a dispersive spectrograph can be seen in Figure 6, where we have convolved our best-fit RIAF and stellar wind models out to $5''$, including ISM extinction effects, with the *NewAthena* X-IFU instrument response function. The model spectra were calculated with an exposure time of 100 ks. Unfortunately, the spatial resolution of *NewAthena* will result in spectral contamination from

³ <https://www.cosmos.esa.int/web/athena/supporting-sci-documents>

both PWN G359.95-0.04 and IRS 13E, which lie a projected distance of approximately $4''$ from Sgr A*. It is unlikely that the signal-to-noise will be high enough to differentiate between the disk and no-disk models, but it may be possible to distinguish between the simplified RIAF model and the predictions of hydrodynamic simulations. In particular, the heightened temperatures anticipated by the stellar wind simulations can be readily tested through the detection of the 6.97 keV Fe XXVI line, which is not predicted by the current RIAF model. The *Lynx*⁴ concept mission is the only concept mission that would significantly advance our understanding of the X-ray emitting accretion flow of Sgr A*. With a spatial resolution approaching $1''$, *Lynx* would be able to isolate Sgr A* from nearby PWN G359.95-0.04 and IRS 13E. The unprecedented sensitivity of *Lynx* would open a completely new window on the Sgr A* accretion flow, possibly allowing for constraints on the bulk and turbulent motions of the hot plasma.

4. SUMMARY & CONCLUSIONS

Besides black hole accretion models, hydrodynamic simulations of shocked plasma from colliding winds of nearby WR stars alone can accurately reproduce the X-ray spectrum of Sgr A*. We investigate whether the formation of a cold accretion disk, seen in both grid-based (Calderón et al. 2020) and particle-based codes (this work), leaves signatures in the gas resolvable by X-ray spectroscopy. The quiescent high-resolution spectrum from the legacy *Chandra*-HETG dataset (PIs: Markoff, Nowak, & Baganoff)⁵ may hint at complex velocity structure in the plasma (Corrales et al. 2020), with possible line shifts close to the maximum line-of-sight velocities predicted by the simulations ($v \sim 1500 \text{ km s}^{-1}$). However, this line structure could be due to extraction techniques or stochastic fluctuations from the relatively high X-ray background.

We compare the HETG-S spectrum to hydrodynamic models that incorporate complicated velocity structure in the dynamic plasma, accounting for the unique geometry and extraction processes of the *Chandra* HETG-S instrument. Building on the work of R17, we examine the X-ray emission from updated simulations of the plasma environment around Sgr A* created by shocked WR stellar winds, using the smoothed particle hydrodynamics (SPH) code GADGET-2, and incorporating updates for the SMBH mass and stellar separations. These models do not consider SMBH feedback but include optically-thin radiative cooling.

We find that the stellar wind plasma cools enough to form a cool disk within the hot accretion flow in both particle-based and grid-based simulations. We are able to reproduce a disk similar to the observed $\sim 10^4$ K H30 α recombination disk (Murchikova et al. 2019) when we run our SPH simulations for 3500 yr. We generate column density, X-ray intensity, and velocity maps for plasma conditions with and without the cold disk. There are minor variations in the X-ray line profiles resulting from the different accretion scenarios, evidenced by slight shifts in the Fe K α peaks. However, these differences are not discernible with the current signal and spectral resolution of the *Chandra* HETG-S.

We compare the predicted X-ray counts histogram from the SPH simulations to a general RIAF model, described in Paper I (Balakrishnan et al. 2024a). We find that the stellar winds make the plasma hotter than predicted by the RIAF. Utilizing Bayesian model evidence to select between models, we find that the RIAF model is weakly preferred. Therefore, hints of a velocity-shifted line complex in the *Chandra* high-resolution HETG spectrum is not proof of complex velocity and temperature structure, but is more likely due to statistical noise. Spectra of Sgr A* taken by the future mission *NewAthena* may be able to differentiate between the RIAF model and stellar wind emission, depending on the strength of the observed 6.97 keV Iron line. Identifying plasma signatures of the cold disk will still be difficult solely with X-ray data. If stellar winds simulations alone, which do not include a feedback mechanism launched from within $10^4 R_g$, sufficiently explain the quiescent X-ray spectrum of Sgr A*, it suggests that accretion stalls in the outer regions of the accretion flow and that feedback is not limited to regions close to the event horizon. This implies that the day-to-day flares from Sgr A* are not necessarily the main drivers of feedback.

While *Chandra* offers the best current combination of spatial and spectral resolution, of all future X-ray missions proposed, only *Lynx* would be able to isolate the Sgr A* accretion flow from its surroundings and provide high enough sensitivity to make significant advances constraining the structure of the Sgr A* accretion flow between 10^4 and $10^6 R_g$.

⁴ <https://www.lynxobservatory.com/mission>

⁵ <https://www.sgra-star.com/>

Software: matplotlib (Hunter 2007), astropy (Astropy Collaboration et al. 2013, 2018), pyatomdb (Foster et al. 2021), pyxis⁶, harmonic (McEwen et al. 2021), gadget-2 (Springel 2005)

1 We would like to thank the referee for their insight-
 2 ful responses, which greatly improved our manuscript.
 3 MB thanks Kayhan Gultekin and Kaze Wong for insight
 4 into model comparison statistics. JC thanks Alex
 5 Gormaz-Matamala for his pointers to the WR abun-
 6 dance literature. The original *Chandra* dataset used
 7 in this work was made possible by the Chandra X-
 8 ray Visionary Program through Chandra Award Num-
 9 ber GO2-13110A, issued by the Chandra X-ray Center
 10 (CXC), which is operated by the Smithsonian Astro-
 11 physical Observatory for NASA under contract NAS8-
 12 03060. Authors MB, CR, and LC were supported by
 13 the CXC grants program, award AR2-23015A and AR2-
 14 23015B. DC is funded by the Deutsche Forschungsge-
 15 meinschaft (DFG, German Research Foundation) under
 16 Germany’s Excellence Strategy – EXC 2121 – ‘Quantum
 17 Universe’ - 390833306. JC acknowledges financial sup-
 18 port from ANID (FONDECYT 1211429 and Millenium
 19 Nucleus TITANS, NCN2023.002). DH acknowledges
 20 funding from the Natural Sciences and Engineering Re-
 21 search Council of Canada (NSERC) and the Canada Re-
 22 search Chairs (CRC) program. Resources supporting
 23 this work were provided by the NASA High-End Com-
 24 puting (HEC) Program through the NASA Advanced
 25 Supercomputing (NAS) Division at Ames Research Cen-
 26 ter.

REFERENCES

- Anders, E., & Grevesse, N. 1989,
 Geochim. Cosmochim. Acta, 53, 197,
 doi: [10.1016/0016-7037\(89\)90286-X](https://doi.org/10.1016/0016-7037(89)90286-X)
- Arnaud, K. A. 1996, in Astronomical Society of the Pacific
 Conference Series, Vol. 101, Astronomical Data Analysis
 Software and Systems V, ed. G. H. Jacoby & J. Barnes,
 17
- Asplund, M., Grevesse, N., Sauval, A. J., & Scott, P. 2009,
 ARA&A, 47, 481,
 doi: [10.1146/annurev.astro.46.060407.145222](https://doi.org/10.1146/annurev.astro.46.060407.145222)
- Astropy Collaboration, Robitaille, T. P., Tollerud, E. J.,
 et al. 2013, A&A, 558, A33,
 doi: [10.1051/0004-6361/201322068](https://doi.org/10.1051/0004-6361/201322068)
- Astropy Collaboration, Price-Whelan, A. M., Sipőcz, B. M.,
 et al. 2018, AJ, 156, 123, doi: [10.3847/1538-3881/aabc4f](https://doi.org/10.3847/1538-3881/aabc4f)
- Baganoff, F. K., Maeda, Y., Morris, M., et al. 2003, ApJ,
 591, 891, doi: [10.1086/375145](https://doi.org/10.1086/375145)
- Begelman, M. C. 2012, MNRAS, 420, 2912,
 doi: [10.1111/j.1365-2966.2011.20071.x](https://doi.org/10.1111/j.1365-2966.2011.20071.x)
- Blandford, R. D., & Begelman, M. C. 1999, MNRAS, 303,
 L1, doi: [10.1046/j.1365-8711.1999.02358.x](https://doi.org/10.1046/j.1365-8711.1999.02358.x)
- Cai, X., McEwen, J. D., & Pereyra, M. 2021, arXiv e-prints,
 arXiv:2106.03646, doi: [10.48550/arXiv.2106.03646](https://doi.org/10.48550/arXiv.2106.03646)
- Calderón, D., Cuadra, J., Schartmann, M., Burkert, A., &
 Russell, C. M. P. 2020, ApJL, 888, L2,
 doi: [10.3847/2041-8213/ab5e81](https://doi.org/10.3847/2041-8213/ab5e81)
- Camilloni, F., Becker, W., & Sasaki, M. 2024, A&A, 681,
 A122, doi: [10.1051/0004-6361/202347970](https://doi.org/10.1051/0004-6361/202347970)
- Canizares, C. R., Davis, J. E., Dewey, D., et al. 2005,
 PASP, 117, 1144, doi: [10.1086/432898](https://doi.org/10.1086/432898)
- Chatterjee, K., Markoff, S., Neilsen, J., et al. 2021,
 MNRAS, 507, 5281, doi: [10.1093/mnras/stab2466](https://doi.org/10.1093/mnras/stab2466)
- Ciurlo, A., Morris, M. R., Campbell, R. D., et al. 2021,
 ApJ, 910, 143, doi: [10.3847/1538-4357/abe71a](https://doi.org/10.3847/1538-4357/abe71a)
- Corrales, L., Baganoff, F. K., Wang, Q. D., et al. 2020,
 ApJ, 891, 71, doi: [10.3847/1538-4357/ab74df](https://doi.org/10.3847/1538-4357/ab74df)
- Corrales, L. R., García, J., Wilms, J., & Baganoff, F. 2016,
 MNRAS, 458, 1345, doi: [10.1093/mnras/stw376](https://doi.org/10.1093/mnras/stw376)

⁶ <https://github.com/eblur/pyxis>

- Cuadra, J., Nayakshin, S., Springel, V., & Di Matteo, T. 2005, *MNRAS*, 360, L55, doi: [10.1111/j.1745-3933.2005.00045.x](https://doi.org/10.1111/j.1745-3933.2005.00045.x)
- Cuadra, J., Nayakshin, S., & Wang, Q. D. 2015, *MNRAS*, 450, 277, doi: [10.1093/mnras/stv584](https://doi.org/10.1093/mnras/stv584)
- Dexter, J., Tchekhovskoy, A., Jiménez-Rosales, A., et al. 2020, *MNRAS*, 497, 4999, doi: [10.1093/mnras/staa2288](https://doi.org/10.1093/mnras/staa2288)
- Eadie, G. M., Speagle, J. S., Cisewski-Kehe, J., et al. 2023, arXiv e-prints, arXiv:2302.04703, doi: [10.48550/arXiv.2302.04703](https://doi.org/10.48550/arXiv.2302.04703)
- Event Horizon Telescope Collaboration, Akiyama, K., Alberdi, A., et al. 2022, *ApJL*, 930, L16, doi: [10.3847/2041-8213/ac6672](https://doi.org/10.3847/2041-8213/ac6672)
- Feroz, F. 2013, in 2013 IEEE 13th International Conference on Data Mining Workshops, 8–15, doi: [10.1109/ICDMW.2013.21](https://doi.org/10.1109/ICDMW.2013.21)
- Feroz, F., Hobson, M. P., & Bridges, M. 2009, *MNRAS*, 398, 1601, doi: [10.1111/j.1365-2966.2009.14548.x](https://doi.org/10.1111/j.1365-2966.2009.14548.x)
- Foster, A. R., Heuer, K., & Smith, R. 2021, in American Astronomical Society Meeting Abstracts, Vol. 53, American Astronomical Society Meeting Abstracts, 228.02
- Fritz, T. K., Gillessen, S., Dodds-Eden, K., et al. 2011, *ApJ*, 737, 73, doi: [10.1088/0004-637X/737/2/73](https://doi.org/10.1088/0004-637X/737/2/73)
- Genzel, R., Eisenhauer, F., & Gillessen, S. 2010, *Reviews of Modern Physics*, 82, 3121, doi: [10.1103/RevModPhys.82.3121](https://doi.org/10.1103/RevModPhys.82.3121)
- Gillessen, S., Genzel, R., Fritz, T. K., et al. 2012, *Nature*, 481, 51, doi: [10.1038/nature10652](https://doi.org/10.1038/nature10652)
- Gillessen, S., Plewa, P. M., Eisenhauer, F., et al. 2017, *ApJ*, 837, 30, doi: [10.3847/1538-4357/aa5c41](https://doi.org/10.3847/1538-4357/aa5c41)
- GRAVITY Collaboration, Abuter, R., Amorim, A., et al. 2019, *A&A*, 625, L10, doi: [10.1051/0004-6361/201935656](https://doi.org/10.1051/0004-6361/201935656)
- Handley, W. J., Hobson, M. P., & Lasenby, A. N. 2015, *MNRAS*, 453, 4384, doi: [10.1093/mnras/stv1911](https://doi.org/10.1093/mnras/stv1911)
- Hunter, J. D. 2007, *Computing in Science & Engineering*, 9, 90, doi: [10.1109/MCSE.2007.55](https://doi.org/10.1109/MCSE.2007.55)
- Jeffreys, H. 1998, *Theory of Probability* (Oxford University Press), doi: [10.1093/oso/9780198503682.001.0001](https://doi.org/10.1093/oso/9780198503682.001.0001)
- Jia, S., Xu, N., Lu, J. R., et al. 2023, *ApJ*, 949, 18, doi: [10.3847/1538-4357/acb939](https://doi.org/10.3847/1538-4357/acb939)
- Lee, M. D., & Wagenmakers, E.-J. 2013, *Bayesian cognitive modeling: A practical course.*, Bayesian cognitive modeling: A practical course. (New York, NY, US: Cambridge University Press), doi: [10.1017/CBO9781139087759](https://doi.org/10.1017/CBO9781139087759)
- Leutenegger, M. A., Cohen, D. H., Zsargó, J., et al. 2010, *ApJ*, 719, 1767, doi: [10.1088/0004-637X/719/2/1767](https://doi.org/10.1088/0004-637X/719/2/1767)
- Lu, J. R., Do, T., Ghez, A. M., et al. 2013, *ApJ*, 764, 155, doi: [10.1088/0004-637X/764/2/155](https://doi.org/10.1088/0004-637X/764/2/155)
- Lützgendorf, N., Helm, E. v. d., Pelupessy, F. I., & Portegies Zwart, S. 2016, *MNRAS*, 456, 3645, doi: [10.1093/mnras/stv2918](https://doi.org/10.1093/mnras/stv2918)
- Ma, R.-Y., Roberts, S. R., Li, Y.-P., & Wang, Q. D. 2019, *MNRAS*, 483, 5614, doi: [10.1093/mnras/sty3039](https://doi.org/10.1093/mnras/sty3039)
- Martins, F., Genzel, R., Hillier, D. J., et al. 2007, *A&A*, 468, 233, doi: [10.1051/0004-6361:20066688](https://doi.org/10.1051/0004-6361:20066688)
- McEwen, J. D., Wallis, C. G. R., Price, M. A., & Spurio Mancini, A. 2021, arXiv e-prints, arXiv:2111.12720, doi: [10.48550/arXiv.2111.12720](https://doi.org/10.48550/arXiv.2111.12720)
- Murchikova, E. M., Phinney, E. S., Pancoast, A., & Blandford, R. D. 2019, *Nature*, 570, 83, doi: [10.1038/s41586-019-1242-z](https://doi.org/10.1038/s41586-019-1242-z)
- Narayan, R., Sądowski, A., Penna, R. F., & Kulkarni, A. K. 2012, *MNRAS*, 426, 3241, doi: [10.1111/j.1365-2966.2012.22002.x](https://doi.org/10.1111/j.1365-2966.2012.22002.x)
- Nogueras-Lara, F., Schödel, R., Gallego-Calvente, A. T., et al. 2020, *Nature Astronomy*, 4, 377, doi: [10.1038/s41550-019-0967-9](https://doi.org/10.1038/s41550-019-0967-9)
- Paumard, T., Genzel, R., Martins, F., et al. 2006, *ApJ*, 643, 1011, doi: [10.1086/503273](https://doi.org/10.1086/503273)
- Peißker, F., Zajaček, M., Thomkins, L., et al. 2023, *ApJ*, 956, 70, doi: [10.3847/1538-4357/acf6b5](https://doi.org/10.3847/1538-4357/acf6b5)
- Price, D. J. 2007, *PASA*, 24, 159, doi: [10.1071/AS07022](https://doi.org/10.1071/AS07022)
- Quataert, E. 2004, *ApJ*, 613, 322, doi: [10.1086/422973](https://doi.org/10.1086/422973)
- Ressler, S. M., Quataert, E., & Stone, J. M. 2018, *MNRAS*, doi: [10.1093/mnras/sty1146](https://doi.org/10.1093/mnras/sty1146)
- . 2020a, *MNRAS*, 492, 3272, doi: [10.1093/mnras/stz3605](https://doi.org/10.1093/mnras/stz3605)
- Ressler, S. M., White, C. J., Quataert, E., & Stone, J. M. 2020b, *ApJL*, 896, L6, doi: [10.3847/2041-8213/ab9532](https://doi.org/10.3847/2041-8213/ab9532)
- Russell, C. M. P., Wang, Q. D., & Cuadra, J. 2017, *MNRAS*, 464, 4958, doi: [10.1093/mnras/stw2584](https://doi.org/10.1093/mnras/stw2584)
- Sander, A. A. C., Hamann, W. R., Todt, H., et al. 2019, *A&A*, 621, A92, doi: [10.1051/0004-6361/201833712](https://doi.org/10.1051/0004-6361/201833712)
- Smith, R. K., Brickhouse, N. S., Liedahl, D. A., & Raymond, J. C. 2001, *ApJL*, 556, L91, doi: [10.1086/322992](https://doi.org/10.1086/322992)
- Solanki, S., Ressler, S. M., Murchikova, L., Stone, J. M., & Morris, M. R. 2023, *ApJ*, 953, 22, doi: [10.3847/1538-4357/acdb6f](https://doi.org/10.3847/1538-4357/acdb6f)
- Springel, V. 2005, *MNRAS*, 364, 1105, doi: [10.1111/j.1365-2966.2005.09655.x](https://doi.org/10.1111/j.1365-2966.2005.09655.x)
- Verner, D. A., & Yakovlev, D. G. 1995, *A&AS*, 109, 125
- von Fellenberg, S. D., Gillessen, S., Graciá-Carpio, J., et al. 2018, *ApJ*, 862, 129, doi: [10.3847/1538-4357/aacd4b](https://doi.org/10.3847/1538-4357/aacd4b)
- Wang, Q. D., Li, J., Russell, C. M. P., & Cuadra, J. 2020, *MNRAS*, 492, 2481, doi: [10.1093/mnras/stz3624](https://doi.org/10.1093/mnras/stz3624)
- Wang, Q. D., Nowak, M. A., Markoff, S. B., et al. 2013, *Science*, 341, 981, doi: [10.1126/science.1240755](https://doi.org/10.1126/science.1240755)

Wilms, J., Allen, A., & McCray, R. 2000, ApJ, 542, 914,
doi: [10.1086/317016](https://doi.org/10.1086/317016)
Xu, Y.-D., Narayan, R., Quataert, E., Yuan, F., &
Baganoff, F. K. 2006, ApJ, 640, 319, doi: [10.1086/499932](https://doi.org/10.1086/499932)
Yuan, F., Quataert, E., & Narayan, R. 2003, ApJ, 598, 301,
doi: [10.1086/378716](https://doi.org/10.1086/378716)

Yusef-Zadeh, F., Royster, M., Wardle, M., et al. 2020,
MNRAS, 499, 3909, doi: [10.1093/mnras/staa2399](https://doi.org/10.1093/mnras/staa2399)